# Structural defects in transition metal dichalcogenide core-shell architectures

Cite as: Appl. Phys. Lett. **118**, 223103 (2021); https://doi.org/10.1063/5.0049121 Submitted: 01 March 2021 . Accepted: 18 May 2021 . Published Online: 03 June 2021







ARTICLES YOU MAY BE INTERESTED IN

Self-intercalated two-dimensional magnetic semiconductor  $V_8(S_{1-X}Se_X)_{15}$ Applied Physics Letters 118, 221903 (2021); https://doi.org/10.1063/5.0049623

Fully epitaxial ferroelectric ScAIN grown by molecular beam epitaxy Applied Physics Letters 118, 223504 (2021); https://doi.org/10.1063/5.0054539

Room temperature depinning of the charge-density waves in quasi-two-dimensional 1T-TaS<sub>2</sub> devices

Applied Physics Letters 118, 223101 (2021); https://doi.org/10.1063/5.0055401

☐ QBLOX



Shorten Setup Time
Auto-Calibration
More Qubits

Fully-integrated
Quantum Control Stacks
Ultrastable DC to 18.5 GHz
Synchronized <<1 ns
Ultralow noise



100s qubits

visit our website >



## Structural defects in transition metal dichalcogenide core-shell architectures

Cite as: Appl. Phys. Lett. 118, 223103 (2021); doi: 10.1063/5.0049121

Submitted: 1 March 2021 · Accepted: 18 May 2021 ·

Published Online: 3 June 2021







Jennifer G. DiStefano, <sup>1,2</sup> (b) Akshay A. Murthy, <sup>1,2</sup> (b) Hee Joon Jung, <sup>1,2,3</sup> (b) Roberto dos Reis, <sup>1,3</sup> (b) and Vinayak P. Dravid <sup>1,2,3,a)</sup> (b)

#### **AFFILIATIONS**

#### **ABSTRACT**

Curvature presents a powerful approach to design atomic structure and tailor material properties in atomically thin transition metal dichalcogenides (TMDs). The emerging TMD core-shell architecture, in which a multilayer TMD shell encapsulates a curved nanoparticle core, presents the opportunity to controllably induce defects into a TMD crystal by strategically constructing the shape of the underlying core. However, harnessing this potential platform first requires robust characterization of the unique structural features present in the coreshell architecture. To this end, transmission electron microscopy (TEM) and scanning TEM (STEM) are particularly powerful tools for direct structural characterization of 2D materials with a high spatial resolution and precision. Here, we reveal and describe defects inherently present in the TMD core-shell architecture. We develop a comprehensive framework to classify the observed defects and discuss potential origins and implications of structural variations. We utilize high resolution S/TEM to reveal the relationship between defects and their associated strain fields. Furthermore, we demonstrate that TMD shells often possess a wide range of interlayer spacings with varied spatial distribution. By exploring the rich array of structural defects inherently present in the TMD core-shell architecture, we provide an important foundation to ultimately induce exotic properties in TMDs through sophisticated defect engineering.

Published under an exclusive license by AIP Publishing. https://doi.org/10.1063/5.0049121

Defects in solids can deteriorate certain materials' properties, but they can also impart unique and useful functionality absent in perfect crystals. Defects play a particularly important role in the properties and behavior of nanostructures and, therefore, a detailed understanding of their influence is critical to developing nanotechnologies. Ultimately, control over defect type, location, and density provides a powerful platform to design advanced nanomaterials. In atomically thin materials, curvature offers a potent method to intrinsically design structure and form localized defects.<sup>2–5</sup> By directly growing transition metal dichalcogenide (TMD) crystals on curved substrates, one could control growth dynamics and deterministically generate localized strain and defects. 6-8 Alternatively, curved TMD nanostructures, such as inorganic fullerenes and nanotubes, naturally possess intriguing structural features and defects, including a range of chiralities, variable registry of concentric shells, size-dependent phase changes, and unusual nanotube capping modalities.<sup>9–12</sup> Revealing these unique structural features and their impact on material properties, such as

mechanical behavior, has enabled the application of inorganic nano-structures in high-strength nanocomposites and solid-state lubrication. <sup>12,13</sup> Comprehensive structural characterization of such complex architectures, particularly via transmission electron microscopy (TEM) and scanning TEM (STEM), is a prerequisite to controllable design of TMD structure and, ultimately, sophisticated property manipulation and defect engineering. <sup>1,14</sup>

Recently, a unique curved TMD structure has emerged—the TMD core-shell architecture, <sup>15</sup> which has already demonstrated potential in optoelectronics, <sup>16–19</sup> energy, <sup>20–25</sup> biomedicine, <sup>26,27</sup> and sensing. <sup>28,29</sup> Unlike its hollow counterparts of inorganic fullerenes and nanotubes, the core-shell is a templated architecture, where a TMD shell encapsulates a rigid nanoparticle core. This structure thus has the benefit of facile hybridization between the functional core and shell materials. Furthermore, it allows for controllable design of strain and defects into the TMD shell through the shape enforced by the underlying core. Through deterministic selection of the core geometry,

Department of Materials Science and Engineering, Northwestern University, Evanston, Illinois 60208, USA

<sup>&</sup>lt;sup>2</sup>International Institute for Nanotechnology (IIN), Northwestern University, Evanston, Illinois 60208, USA

<sup>&</sup>lt;sup>3</sup>Northwestern University Atomic and Nanoscale Characterization Experimental (NUANCE) Center, Northwestern University, Evanston, Illinois 60208, USA

<sup>&</sup>lt;sup>a)</sup>Author to whom correspondence should be addressed: v-dravid@northwestern.edu

superior control of structure and defects in TMDs is possible via the core-shell architecture.

Exquisite structural understanding and control would make the TMD core-shell architecture a ripe platform for defect engineering and enable powerful synergistic effects such as strategic hybridization coupled with defects to induce unique topological properties. However, work remains to build a robust set of design rules that consider the complexity (e.g., curvature, multiple interfaces, and multiplayer nature) of the TMD core-shell architecture and predict the exact nature of the shell structure. Diverse morphologies of TMD core-shell structures have been documented previously, but the underlying defects and structural variations have not yet been examined. Detailed characterization of the defects and local strain fields in these unique core-shell architectures could shed light on the inherent structure—which in turn impacts physical properties—and offer routes for future structural control.

In this work, we aim to elucidate the nanoscale and interfacial structure of the TMD core-shell architecture using high-resolution S/TEM. The scope of this work includes thoroughly describing and documenting defects through structural characterization. We first report on a series of defects observed in TMD core-shells using compiled data from multiple core-shell material combinations. We classify these observed structures spatially within the core-shell—at the core/ shell interface, the shell surface, or internal to the shell—to provide an overview of the possible structural variations. We then conduct detailed S/TEM analyses on select defects within the TMD shell, with a focus on their structural complexity and the localized effects of defective regions such as local strain fields. Finally, we examine the distribution of interlayer spacings in the TMD shell. By probing the detailed structure within the TMD core-shell architecture, this work lays the foundation to ultimately utilize curvature to engineer targeted defects into TMDs.

We consider data from 16 chemical vapor deposition (CVD) TMD core-shell samples of various sizes, shapes, and core materials to produce a comprehensive framework of the defects intrinsically present in this generalized architecture (Fig. 1). We categorize these defects into three key regions of the core-shell architecture: the heterogeneous core/shell interface, the shell surface, and the internal shell. S/TEM images demonstrating examples of defects in each region are presented in Figs. 2–4 or Fig. S1.

The core/shell interface category considers the growth of the initial TMD layer around a nanoparticle core. The nature of this interface dictates the level of atomic and molecular hybridization present between core and shell constituents and thus plays a crucial role in the associated emergent phenomena present in these systems. <sup>30,31</sup> An intimate core/shell interface maximizes the interaction between the two materials and is achieved through conformal encapsulation [Fig. 1(a)]. Conformal interfaces in TMD core-shell geometries have previously enabled enhanced and unusual properties such as plasmonic enhancement and increased hydrogen production. <sup>16,19,24</sup> The conformal shell is commonly observed in CVD TMD core-shell literature and serves as the basis for the subsequent two categories. <sup>16–18,32</sup>

Core/shell interfaces that disrupt complete contact between the core and shell could limit the extent of hybridization between the two materials but also introduce their own unique functionality. In the shell facet interface, the initial layer of the shell loses contact with a region of the core [Fig. 1(b)]. This interface type might be attributable

### CORE/SHELL INTERFACE (a) Conformal Shell Facet **Exposed Core SHELL SURFACE** (e) (g) Complete Incomplete Delaminated Mismatched **External Shell** External Shell External Shell Intersection **INTERNAL SHELL** (i)

**FIG. 1.** TMD core-shell defect classification framework. (a)–(c) Structural variations at the core/shell interface, which determines the potential for hybridization between core and shell materials. (d)–(g) Structural variations at the shell surface, which strongly affects the interaction between a core-shell structure and its environment and opens opportunities for chemical functionalization. (h)–(k) Structural variations within the TMD shell, which dictates the rate at which events such as diffusion, charge transport, and intercalation can proceed.

**Shell Facet** 

Gap in Shell

Incomplete

Continued

Conformal

to extreme curvature, as will be discussed later in more detail. An incomplete shell could also form, leaving a section of the core exposed [Fig. 1(c)], as observed in other core-shell preparation methods. <sup>20,33</sup> In CVD, the comparative interfacial energies between the core, shell, and substrate materials largely dictate the completeness of encapsulation and could explain this defect. <sup>34</sup> For instance, if the interfacial energy between the TMD and substrate material is low, it may be more favorable for the TMD to grow along the substrate surface than between the core and substrate, resulting in partial encapsulation. The incomplete shell interface is not ideal for hybridization, but it could enable alternate engineering avenues such as formation of Janus-like particles, where each surface (i.e., shell and exposed core) provides distinct chemistries and molecular attachment opportunities. <sup>35–37</sup>

The second category in the defect framework is the shell surface, which involves termination of the final TMD layer(s) in the shell. The shell termination mode is particularly important for controlling how the core-shell structure interacts with its environment. Specifically, TMD edges contain reactive dangling bonds while the basal plane does not.<sup>38</sup> The framework includes shell surface structures without dangling bonds [Fig. 1(d)], where all bonds are satisfied in-plane, and with dangling bonds [Figs. 1(e)–1(g)]. An incomplete external shell [schematic in Fig. 1(e), TEM image in Fig. 2(b)], and the related delaminated external shell [Fig. 1(f)], would likely arise due to the exhaustion of precursors during a synthesis process, leaving at least one layer unfinished. Furthermore, mismatched intersections of TMD layers, or shell discontinuities, often occur at sharp facets in the core

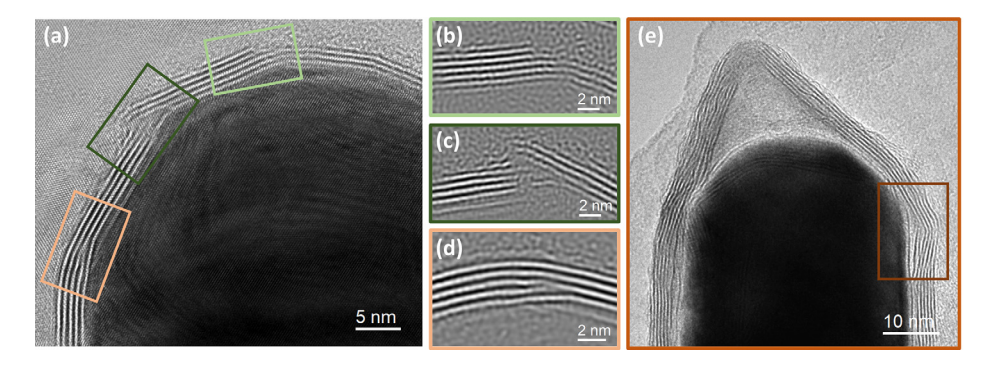


FIG. 2. Defects at the TMD shell surface and within the shell. (a) TEM image of semi-spherical Au@MoS<sub>2</sub> core-shell containing the defects presented in (b)–(d). (b)–(d) Filtered TEM images of incomplete external shell, mismatched intersection, and incomplete internal shell defects, respectively. (e) TEM image of an Au nanorod@MoS<sub>2</sub> core-shell structure exhibiting a shell facet. Orange box indicates a gap in shell defect.

[Fig. 1(g)]. A TEM image of a mismatched intersection [Fig. 2(c)] shows a discontinuous shell termination. The two edges of the shell are possibly not as aligned in the z-direction as they appear in projection, but a severe discontinuity clearly exists in the region. Such an edge-dominated termination mode has implications for many catalysis applications that can leverage the increased reactivity of the exposed TMD edge sites. 38–40

The remainder of this work considers the rich array of features possible within the TMD shell. In this region of the nanostructure, critical functions such as energy transfer, charge transport, diffusion, and intercalation occur. Continued conformal growth [Fig. 1(h)] occurs when each TMD layer is complete and concentric around the underlying layer, analogous to pristine lamellar growth in a planar TMD geometry. A potential deviation from conformal growth is an incomplete inner shell [Fig. 1(i)]. Figure 2(d) exhibits an incomplete inner layer that appears to abruptly terminate in the shell interior, similar to edge-like defects previously observed in layered materials. <sup>41</sup> We hypothesize that local growth dynamics, rather than precursor exhaustion, are responsible for this defect. A high density of local nucleation sites, known to occur under certain CVD conditions, could cause

neighboring layers to grow above an incomplete inner layer and limit precursor diffusion to the unfinished layer. <sup>15</sup>

The Au nanorod encapsulated by an MoS2 shell in Fig. 2(e) demonstrates two additional internal shell variations. Faceting in the shell [Fig. 1(j)] is apparent at the nanorod endcap, where conformal MoS<sub>2</sub> layers first encapsulate the nanorod core, then a gap is introduced as the shell forms a facet and subsequent shell layers grow accordingly. These facets, and the related shell facets at the core/shell interface, primarily occur at the endcaps of nanorods rather than along the sides. This is consistent with observations of structural defects in inorganic nanotubes forming primarily in the endcaps. The shell surrounding the straight center of a nanorod is curved only in one direction (around the rod), whereas a conformal shell at the endcaps is curved in two directions, forming a positive curvature. As a result, the strain due to bending is higher at the endcaps than along the sides. 42 Such a high strain environment leads to energy relaxation through defect formation once a certain critical thickness and curvature are reached. This could explain the transition from curved conformal internal layers to faceted outer layers exclusively at the endcap. Similarly, defect-rich TMD shells in core-shell structures have previously been

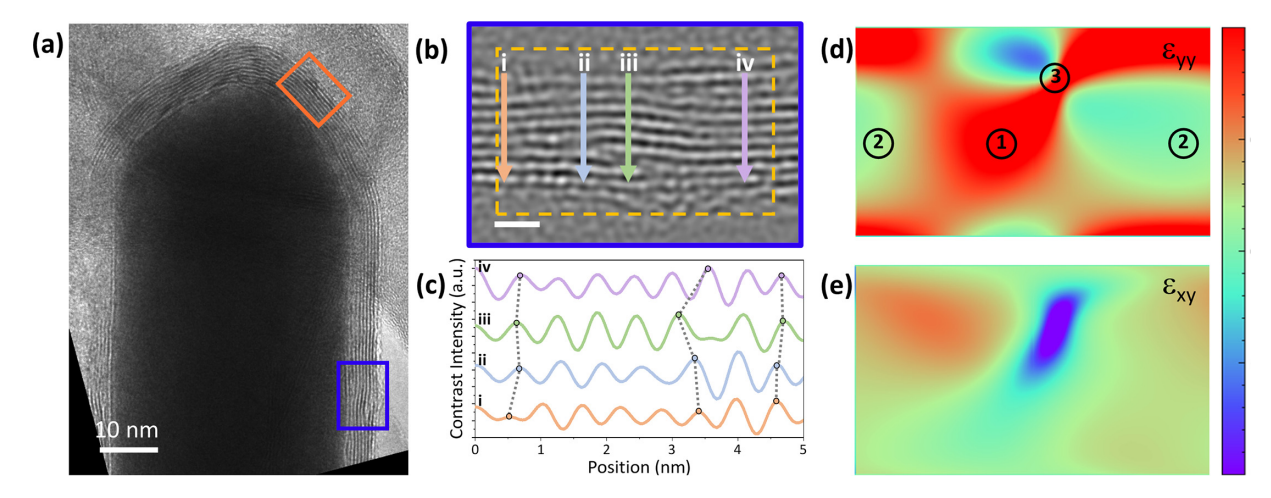


FIG. 3. The impact of defective regions within the TMD shell. (a) BF TEM image of an Au nanorod with a multilayer  $MoS_2$  shell. (b) Band pass Fourier filtered BF TEM image of the region of the  $MoS_2$  shell marked by the blue box in (a), indicating several intersecting incomplete internal layers. Scale bar represents 2 nm. (c) Contrast line profiles of the defective shell region, corresponding to the lines labeled in (b). Dotted lines indicate the loss of registry between layers near the defects. (d) Relative out-of-plane and (e) shear strain maps of the region indicated by the yellow box in (b) obtained using GPA. The numbers indicate features discussed in the text. The color bar indicates +/- 1% strain compared to the reference region (see Fig. S3).

observed at regions of high curvature.<sup>20</sup> As such, this feature could shed light on the growth dynamics and strain state of TMD shells of various thicknesses and curvatures.

Finally, an unusually large gap between adjacent layers [Fig. 1(k)] is observed along the edge of the encapsulated nanorod [orange box in Fig. 2(e)]. This feature is similar to buckling layers previously reported in planar layered materials due to accommodation of strain, leading to out-of-plane relaxation. 43,44 Several scenarios could explain the origin of compressive stress expected to form this gap. 43 One possibility is the addition of molecular units in the layer where the gap initiated. The nature of TMD core-shells: (1) requires that each layer contains more TMD molecular units than the prior to continue concentric encapsulation and maintain similar strain states among layers and (2) constrains each layer into forming a closed shell. Given this complexity, it is unlikely that each new layer possesses the exact number of TMD units needed to produce a perfectly conformal, closed shell. Compressive stresses result when molecular units are added and could cause gap formation within the shell. The stress needed to form this gap could also originate from a nearby dislocation, such as when internal layers abruptly terminate, straining the above layers until they regain their expected spacing.

We next consider how defective regions in the shell can modify local structure and introduce strain fields by examining a defective region in an Au nanorod@MoS<sub>2</sub> nanoparticle [Fig. 3(a)]. Figure 3(b) shows a defective shell region with several intersecting incomplete layers, corresponding to the blue box in Fig. 3(a). An analysis of a relatively defect-free region [orange box in Fig. 3(a)] is shown in Fig. S2 for comparison. Contrast intensity line profiles [Fig. 3(c)] are collected at several points to demonstrate how these defects impact interlayer spacing and layer registry. The additional peak in line profile iv [to the right of the defective region in Fig. 3(b)] indicates that a new layer is present compared to line profile i (left of the defective region). Defects can thus be accompanied by the presence of extra TMD layers, affecting the interlayer separation and producing localized strain fields, which could further disrupt long-range order.

We utilize a geometric phase analysis (GPA) approach to examine the qualitative strain fields induced by the defective region.<sup>45</sup> It is important to note that these strain signs and magnitudes are relative to a reference region (see the supplementary material). Out-of-plane  $(\varepsilon_{vv})$  and shear  $(\varepsilon_{xv})$  strain maps [Figs. 3(d) and 3(e)] both demonstrate discontinuity concentrated near the defective region. The outof-plane strain field is highly tensile with the largest values occurring in the immediate region of the half-layer termination (labeled as point 1). Furthermore, compression after the addition of a new layer is apparent by comparing the strains on either side of the defective region (point 2) in both the  $\varepsilon_{yy}$  and  $\varepsilon_{xy}$  maps. Additionally, the compressive to tensile feature in the  $\varepsilon_{yy}$  strain map (point 3) can be attributed to the abrupt layer displacement observed in the image, compared to the more gradual accommodation of an additional halfplane near the center defects. Understanding local strain associated with such defects is key to eventually access desirable-and avoid undesirable—strain-induced effects in TMD core-shells such as photocarrier confinement, exciton funneling, and bandgap engineering.

The final component of structure we consider is the interlayer spacing between TMD layers in the shell. Tuning the interlayer spacing of van der Waals materials, including TMDs, can modify factors such as the intercalation/de-intercalation rates, adsorption/desorption

energies, and coupling strength between adjacent layers, all of which have important implications for applications including energy storage, catalysis, environmental remediation, and electronics. <sup>50–54</sup> Curvature is known to impact the interlayer spacing of TMDs, <sup>9</sup> making it an important parameter to investigate in complex curved nanostructures such as the core-shell architecture.

Analysis of a 50+ layer  $MoS_2$  shell from an  $Au@MoS_2$  structure (Fig. S4) reveals interesting irregularities in layer spacing. A BF STEM image of the region of interest and the associated Bragg image are shown in Figs. 4(a) and 4(b). Several topological defects are apparent in the shell, including edge-like, kink, and knot defects highlighted in Figs. 4(c)–4(e). An interlayer spacing map [Fig. 4(f)] of the region indicates spacings with a broad range of 0.16 nm. Only the relative spacings were considered here (see Methods), and zero represents the average interlayer spacing of the region. These data suggest that layers exhibit variable interlayer spacing across their length. Overlays of several topological defects and their associated interlayer spacings are shown in Figs. 4(g)–4(i). While there is strong correlation between the

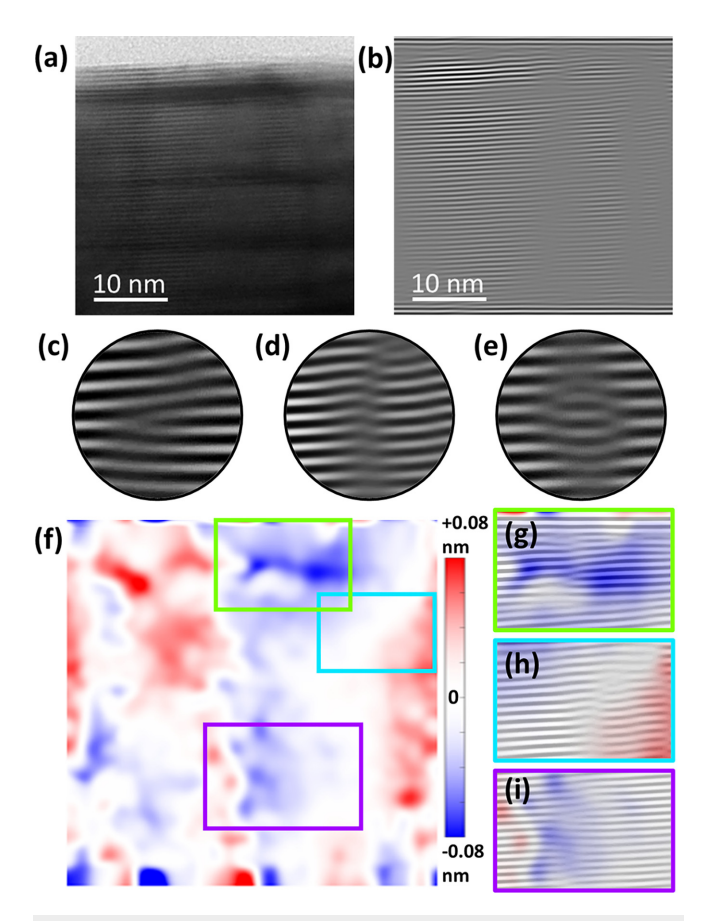


**FIG. 4.** Interlayer spacing in  $Au@MoS_2$  core-shell structures. (a) BF STEM micrograph of a thick  $MoS_2$  shell region in an  $Au@MoS_2$  core-shell particle. (b) Bragg image formed from (a) (see Fig. S4). (c)–(e) Magnified topological defects demonstrating an edge-like defect, kink, and knot, respectively. (f) A 2D map of the lattice spacing variation in (a). The mean lattice spacing value corresponds to 0, indicating a wide range of +/- 0.08 nm in this region. (g)–(i) Overlays of the Bragg image and the lattice spacing map, corresponding to the colored boxes shown in (f).

observed defects and changes in interlayer spacing, such defects do not account for all variation observed in Fig. 4(f). As such, we hypothesize that the presence of defects that are not visible contribute to localized variations in interlayer spacing and related strains. The associated strain maps (Fig. S5) demonstrate how the inhomogeneity in interlayer spacing within the shell affects local strain distributions, with high values around the core of defects in  $\varepsilon_{xx}$  and  $\varepsilon_{yy}$ . Furthermore, a quantitative analysis of an Au@MoS2 structure (Fig. S6) demonstrates MoS2 interlayer spacings ranging from 0.63 to 0.70 nm, consistently higher than the expected interlayer spacing of 2H MoS2 (0.61–0.62). These analyses indicate both an increased average interlayer spacing compared to planar MoS2 and significant local variations within the shell and suggest that core-shell geometries could serve as a platform to controllably tune interlayer spacing for a range of applications.

In this work, we document and catalogue structural variations in the TMD core-shell architecture and utilize S/TEM to examine these defects in detail regardless of their origin. We identify rich structural variety inherent to this architecture, with features spanning multiple interfaces and dimensionalities. Some features, such as edge-like defects, have been previously observed in layered materials while others that have not yet been examined could hold promise for emergent properties. Furthermore, we find that TMD core-shell structures exhibit a wide range of interlayer spacings, which tend to be larger than those of planar TMDs. Overall, this work elucidates that key features for property tunability naturally manifest in curved TMD architectures. As such, ample opportunity awaits to further probe the structure of TMD core-shells. Establishing a robust understanding of the relationship between curvature, synthesis conditions, and structure will enable advanced defect engineering in TMD core-shell architectures and pave the way for exploiting their many unusual features.

See the supplementary material for methods and additional S/TEM analyses.

This material is based upon work primarily supported by the National Science Foundation (NSF) under Grant No. DMR-1929356 and partially supported by the Air Force Office of Scientific Research under Grant No. FA9550-17-1-0348-P00003 and Army Research Office Grant No. W911NF1910335. This work made use of the EPIC facility of Northwestern University's NUANCE Center, which has received support from the SHyNE Resource (NSF ECCS-2025633), the IIN, and Northwestern's MRSEC program (NSF DMR-1720139).

#### DATA AVAILABILITY

The data that support the findings of this study are available from the corresponding author upon reasonable request.

#### **REFERENCES**

- <sup>1</sup>P. B. Hirsch, A. Howie, R. B. Nicholson, D. W. Pashley, and M. J. Whelan, "Electron microscopy of thin crystals," Acta Crystallogr. **21**, 454–454 (1966).
- <sup>2</sup>W. T. M. Irvine, V. Vitelli, and P. M. Chaikin, "Pleats in crystals on curved surfaces," Nature 468, 947–951 (2010).
- <sup>3</sup>H. Terrones and M. Terrones, "Curved nanostructured materials," New J. Phys. 5, 126–137 (2003).
- <sup>4</sup>C. Köhler, R. Backofen, and A. Voigt, "Stress induced branching of growing crystals on curved surfaces," Phys. Rev. Lett. 116, 135502 (2016).

- <sup>5</sup>G. Meng, J. Paulose, D. R. Nelson, and V. N. Manoharan, "Elastic instability of a crystal growing on a curved surface," Science 343, 634–637 (2014).
- <sup>6</sup>K. Wang, A. A. Puretzky, Z. Hu, B. R. Srijanto, X. Li, N. Gupta, H. Yu, M. Tian, M. Mahjouri-Samani, X. Gao *et al.*, "Strain tolerance of two-dimensional crystal growth on curved surfaces," Sci. Adv. 5, eaav4028 (2019).
- <sup>7</sup>H. Yu, N. Gupta, Z. Hu, K. Wang, B. R. Srijanto, K. Xiao, D. B. Geohegan, and B. I. Yakobson, "Tilt grain boundary topology induced by substrate topography," ACS Nano 11, 8612–8618 (2017).
- <sup>8</sup>Y. Wang and V. H. Crespi, "Theory of finite-length grain boundaries of controlled misfit angle in two-dimensional materials," Nano Lett. 17, 5297–5303 (2017)
- <sup>9</sup>M. Krause, A. Mücklich, A. Zak, G. Seifert, and S. Gemming, "High resolution TEM study of WS<sub>2</sub> nanotubes," Phys. Status Solidi Basic Res. **248**, 2716–2719 (2011).
- <sup>10</sup> M. B. Sadan, L. Houben, A. N. Enyashin, G. Seifert, R. Tenne, and S. G. Louie, "Atom by atom: HRTEM insights into inorganic nanotubes and fullerene-like structures," Proc. Natl. Acad. Sci. U. S. A. 105, 15643–15648 (2008).
- <sup>11</sup>F. L. Deepak, A. Mayoral, A. J. Steveson, S. Mejía-Rosales, D. A. Blom, and M. José-Yacamán, "Insights into the capping and structure of MoS<sub>2</sub> nanotubes as revealed by aberration-corrected STEM," Nanoscale 2, 2286–2293 (2010).
- <sup>12</sup>M. Bar Sadan, M. Heidelmann, L. Houben, and R. Tenne, "Inorganic WS<sub>2</sub> nanotubes revealed atom by atom using ultra-high-resolution transmission electron microscopy," Appl. Phys. A 96, 343–348 (2009).
- <sup>13</sup>B. Višić, L. S. Panchakarla, and R. Tenne, "Inorganic nanotubes and fullerene-like nanoparticles at the crossroads between solid-state chemistry and nanotechnology," J. Am. Chem. Soc. 139, 12865–12878 (2017).
- 14D. B. Williams and C. B. Carter, Transmission Electron Microscopy, 2nd ed. (Springer, 2009).
- <sup>15</sup>J. G. DiStefano, A. A. Murthy, S. Hao, R. Dos Reis, C. Wolverton, and V. P. Dravid, "Topology of transition metal dichalcogenides: The case of the coreshell architecture," Nanoscale 12, 23897–23919 (2020).
- <sup>16</sup>Y. Li, J. G. DiStefano, A. A. Murthy, J. D. Cain, E. D. Hanson, Q. Li, F. C. Castro, X. Chen, and V. P. Dravid, "Superior plasmonic photodetectors based on Au@MoS<sub>2</sub> core-shell heterostructures," ACS Nano 11, 10321–10329 (2017).
- <sup>17</sup>J. G. DiStefano, Y. Li, H. J. Jung, S. Hao, A. A. Murthy, X. Zhang, C. Wolverton, and V. P. Dravid, "Nanoparticle@MoS<sub>2</sub> core—shell architecture: Role of the core material," Chem. Mater. 30, 4675–4682 (2018).
- <sup>18</sup>Y. Li, J. D. Cain, E. D. Hanson, A. A. Murthy, S. Hao, F. Shi, Q. Li, C. Wolverton, X. Chen, and V. P. Dravid, "Au@MoS<sub>2</sub> core-shell heterostructures with strong light-matter interactions," Nano Lett. 16, 7696–7702 (2016).
- <sup>19</sup>Z. Li, S. Jiang, Y. Huo, A. Liu, C. Zhang, J. Yu, M. Wang, C. Li, Z. Lu, and B. Man, "3D hybrid plasmonic nanostructures with dense hot spots using monolayer MoS<sub>2</sub> as sub-nanometer spacer," Adv. Mater. Interfaces 5, 1800661 (2018).
- <sup>20</sup>R. Bar-Ziv, P. Ranjan, A. Lavie, A. Jain, S. Garai, A. Bar Hen, R. Popovitz-Biro, R. Tenne, R. Arenal, A. Ramasubramaniam *et al.*, "Au-MoS<sub>2</sub> hybrids as hydrogen evolution electrocatalysts," ACS Appl. Energy Mater. 2, 6043–6050 (2019).
- <sup>21</sup>N. Li, Z. Liu, Q. Gao, X. Li, R. Wang, X. Yan, and Y. Li, "In Situ synthesis of concentric C@MoS<sub>2</sub> core-shell nanospheres as anode for lithium ion battery," J. Mater. Sci. 52, 13183–13191 (2017).
- <sup>22</sup>H. Ma, S. Du, H. Tao, T. Li, and Y. Zhang, "Three-dimensionally integrated carbon tubes/MoS<sub>2</sub> with reduced graphene oxide foam as a binder-free anode for lithium ion battery," J. Electroanal. Chem. 823, 307–314 (2018).
- <sup>23</sup>Y. Li, M. Majewski, S. Islam, S. Hao, A. Murthy, J. DiStefano, E. Hanson, Y. Xu, C. Wolverton, M. Kanatzidis *et al.*, "Morphological engineering of winged Au@MoS<sub>2</sub> heterostructures for electrocatalytic hydrogen evolution," Nano Lett. 18, 7104–7110 (2018).
- <sup>24</sup>P. S. Maiti, A. K. Ganai, R. Bar-Ziv, A. N. Enyashin, L. Houben, and M. Bar-Sadan, "Cu<sub>2-x</sub>S-MoS<sub>2</sub> nano-octahedra at the atomic scale: Using a template to activate the basal plane of MoS<sub>2</sub> for hydrogen production," Chem. Mater. 30, 4489–4492 (2018).
- 25K. Chen, S.-J. Ding, Z.-J. Luo, G.-M. Pan, J.-H. Wang, J. Liu, L. Zhou, and Q.-Q. Wang, "Largely enhanced photocatalytic activity of Au/XS<sub>2</sub>/Au (X = Re, Mo) antenna-reactor hybrids: Charge and energy transfer," Nanoscale 10, 4130-4137 (2018).
- 26 S. K. Maji, S. Yu, K. Chung, and M. S. Ramasamy, "Synergistic nanozymetic activity of hybrid gold bipyramid—molybdenum disulfide core@shell

- nanostructures for two-photon imaging and anticancer therapy," ACS Appl. Mater. Interfaces 10, 42068–42076 (2018).
- 27 R. Prakash and N. R. Nirala, "One step synthesis of AuNPs@MoS<sub>2</sub>-QDs composite as a robust peroxidas-mimetic for instant unaided eye detection of glucose in serum, saliva, and tear," Sens. Actuators B 263, 109–119 (2018).
- <sup>28</sup>X. Fei, Z. Liu, Y. Hou, Y. Li, G. Yang, C. Su, Z. Wang, H. Zhong, Z. Zhuang, and Z. Guo, "Synthesis of Au NP@MoS<sub>2</sub> quantum dots core@shell nanocomposites for SERS bio-analysis and label-free bio-imaging," Materials 10, 650 (2017).
- <sup>29</sup>S. Guo, X. Ren, and X. Li, "Au@MoS2@Au hierarchical nanostructures for high-sensitivity and recyclable SERS device," Plasmonics 15, 591–598 (2020).
- 30S. Lepeshov, M. Wang, A. Krasnok, O. Kotov, T. Zhang, H. Liu, T. Jiang, B. Korgel, M. Terrones, Y. Zheng et al., "Tunable resonance coupling in single Si nanoparticle—monolayer WS<sub>2</sub> structures," ACS Appl. Mater. Interfaces 10, 16690–16697 (2018).
- <sup>31</sup>H. Wang, J. Wen, W. Wang, N Xu, P. Liu, J. Yan, H. Chen, and S. Deng, "Resonance coupling in heterostructures composed of silicon nanosphere and monolayer WS<sub>2</sub>: A magnetic-dipole-mediated energy transfer process," ACS Nano 13, 1739–1750 (2019).
- <sup>32</sup>X. Chen, H. Yang, G. Liu, F. Gao, M. Dai, Y. Hu, H. Chen, W. Cao, P. Hu, and W. Hu, "Hollow spherical nanoshell arrays of 2D layered semiconductor for high-performance photodetector device," Adv. Funct. Mater. 28, 1705153 (2018).
- 33 J. G. DiStefano, A. A. Murthy, C. J. Lescott, R. dos Reis, Y. Li, and V. P. Dravid, "Au@MoS2@WS2 core-shell architectures: Combining vapor phase and solution-based approaches," J. Phys. Chem. C 124, 2627–2633 (2020).
- 34Y. Li, S. Hao, J. DiStefano, A. Murthy, E. Hanson, Y. Xu, C. Wolverton, X. Chen, and V. Dravid, "Site-specific positioning and patterning of MoS<sub>2</sub> monolayers: The role of Au seeding," ACS Nano 12, 8970–8976 (2018).
- <sup>35</sup>G. Agrawal and R. Agrawal, "Janus nanoparticles: Recent advances in their interfacial and biomedical applications," ACS Appl. Nano Mater. 2, 1738–1757 (2019).
- 36 J. Hu, S. Zhou, Y. Sun, X. Fang, and L. Wu, "Fabrication, properties and applications of Janus particles," Chem. Soc. Rev. 41, 4356–4378 (2012).
- <sup>37</sup>Q. Chen, J. Yan, J. Zhang, S. C. Bae, and S. Granick, "Janus and multiblock colloidal particles," Langmuir 28, 13555–13561 (2012).
- <sup>38</sup>G. Li, D. Zhang, Q. Qiao, Y. Yu, D. Peterson, A. Zafar, R. Kumar, S. Curtarolo, F. Hunte, S. Shannon *et al.*, "All the catalytic active sites of MoS<sub>2</sub> for hydrogen evolution," J. Am. Chem. Soc. 138, 16632–16638 (2016).
- <sup>39</sup>M. Asadi, B. Kumar, A. Behranginia, B. A. Rosen, A. Baskin, N. Repnin, D. Pisasale, P. Phillips, W. Zhu, R. Haasch *et al.*, "Robust carbon dioxide reduction on molybdenum disulphide edges," Nat. Commun. 5, 4470 (2014).
- <sup>40</sup>J. Kibsgaard, Z. Chen, B. N. Reinecke, and T. F. Jaramillo, "Engineering the surface structure of MoS<sub>2</sub> to preferentially expose active edge sites for electrocatalysis," Nat. Mater. 11, 963–969 (2012).
- <sup>41</sup>R. K. Vasudevan, S. M. Neumayer, M. A. Susner, M. A. McGuire, S. T. Pantelides, P. Maksymovych, D. N. Leonard, N. Balke, and A. Y. Borisevich, "Domains and topological defects in layered ferrielectric materials: Implications for nanoelectronics," ACS Appl. Nano Mater. 3, 8161–8166 (2020).

- <sup>42</sup>A. Enyashin and G. Seifert, "Inorganic fullerenes and nanotubes," in *Handbook of Nanophysics: Nanotubes & Nanowires* (CRC Press LLC, 2010), pp. 1–21.
- <sup>43</sup>A. Kushima, X. Qian, P. Zhao, S. Zhang, and J. Li, "Ripplocations in van Der Waals layers," Nano Lett. 15, 1302–1308 (2015).
- <sup>44</sup>B. Butz, C. Dolle, F. Niekiel, K. Weber, D. Waldmann, H. B. Weber, B. Meyer, and E. Spiecker, "Dislocations in bilayer graphene," Nature 505, 533–537 (2014).
- 45M. J. Hÿtch, E. Snoeck, and R. Kilaas, "Quantitative measurement of displacement and strain fields from HREM micrographs," Ultramicroscopy 74, 131–146 (1998).
- <sup>46</sup>B. G. Shin, G. H. Han, S. J. Yun, H. M. Oh, J. J. Bae, Y. J. Song, C.-Y. Park, and Y. H. Lee, "Indirect bandgap puddles in monolayer MoS<sub>2</sub> by substrate-induced local strain," Adv. Mater. 28, 9378–9384 (2016).
- <sup>47</sup>A. Castellanos-Gomez, R. Rolda, E. Cappelluti, M. Buscema, F. Guinea, H. S. J. van der Zant, and G. A. Steele, "Local strain engineering in atomically thin MoS<sub>2</sub>," Nano Lett. 13, 5361–5366 (2013).
- <sup>48</sup>L. Chirolli, E. Prada, F. Guinea, R. Roldán, and P. San-Jose, "Strain-induced bound states in transition-metal dichalcogenide bubbles," 2D Mater. 6, 025010 (2019).
- 49A. Branny, S. Kumar, R. Proux, and B. D. Gerardot, "Deterministic strain-induced arrays of quantum emitters in a two-dimensional semiconductor," Nat. Commun. 8, 15053 (2017).
- 50 K. D. Rasamani, F. Alimohammadi, and Y. Sun, "Interlayer-expanded MoS<sub>2</sub>," Mater. Today 20, 83–91 (2017).
- 51Y. Gong, H. Yuan, C. L. Wu, P. Tang, S. Z. Yang, A. Yang, G. Li, B. Liu, J. Van De Groep, M. L. Brongersma *et al.*, "Spatially controlled doping of twodimensional SnS<sub>2</sub> through intercalation for electronics," Nat. Nanotechnol. 13, 294–299 (2018).
- 52K. Ai, C. Ruan, M. Shen, and L. Lu, "MoS<sub>2</sub> nanosheets with widened interlayer spacing for high-efficiency removal of mercury in aquatic systems," Adv. Funct. Mater. 26, 5542–5549 (2016).
- <sup>53</sup>S. Zhang, B. V. R. Chowdari, Z. Wen, J. Jin, and J. Yang, "Constructing highly oriented configuration by few-layer MoS<sub>2</sub>: Toward high-performance lithiumion batteries and hydrogen evolution reactions," ACS Nano 9, 12464–12472 (2015).
- 54Y. J. Tang, Y. Wang, X. L. Wang, S. L. Li, W. Huang, L. Z. Dong, C. H. Liu, Y. F. Li, and Y. Q. Lan, "Molybdenum disulfide/nitrogen-doped reduced graphene oxide nanocomposite with enlarged interlayer spacing for electrocatalytic hydrogen evolution," Adv. Energy Mater. 6, 1600116 (2016).
- 55K. Wu, X. Cao, M. Li, B. Lei, J. Zhan, and M. Wu, "Bottom-up synthesis of MoS<sub>2</sub>/CNTs hollow polyhedron with 1T/2H hybrid phase for superior potassium-ion storage," Small 16, 2004178 (2020).
- 56N. Kumar, E. Fosso-Kankeu, and S. S. Ray, "Achieving controllable MoS<sub>2</sub> nanostructures with increased interlayer spacing for efficient removal of Pb(II) from aquatic systems," ACS Appl. Mater. Interfaces 11, 19141–19155 (2019).
- <sup>57</sup>C. Wu, H. Song, C. Tang, A. Du, C. Yu, Z. Huang, M. Wu, and H. Zhang, "Ultralarge interlayer distance and C,N-codoping enable superior sodium storage capabilities of MoS<sub>2</sub> nanoonions," Chem. Eng. J. 378, 122249 (2019).